How to cite: *Angew. Chem. Int. Ed.* **2023**, *62*, e202301920
doi.org/10.1002/anie.202301920

CO Oxidation

Unveiling the CO Oxidation Mechanism over a Molecularly Defined Copper Single-Atom Catalyst Supported on a Metal–Organic Framework

Ali M. Abdel-Mageed, Bunyarat Rungtaweevoranit,* Sarawoot Impeng,* Joachim Bansmann, Jabor Rabeah, Shilong Chen, Thomas Häring, Supawadee Namuangrak, Kajornsak Faungnawakij, Angelika Brückner, and R. Jürgen Behm**

Abstract: Elucidating the reaction mechanism in heterogeneous catalysis is critically important for catalyst development, yet remains challenging because of the often unclear nature of the active sites. Using a molecularly defined copper single-atom catalyst supported by a UiO-66 metal–organic framework (Cu/UiO-66) allows a detailed mechanistic elucidation of the CO oxidation reaction. Based on a combination of in situ/operando spectroscopies, kinetic measurements including kinetic isotope effects, and density-functional-theory-based calculations, we identified the active site, reaction intermediates, and transition states of the dominant reaction cycle as well as the changes in oxidation/spin state during reaction. The reaction involves the continuous reactive dissociation of adsorbed O_2, by reaction of $O_{2,ad}$ with CO_{ad}, leading to the formation of an O atom connecting the Cu center with a neighboring Zr^{4+} ion as the rate limiting step. This is removed in a second activated step.

Introduction

The identification of the active site(s) is a prerequisite for a comprehensive mechanistic understanding of catalytic reactions and for the systematic control of the catalyst performance.[1] For most realistic technical heterogeneous catalysts this is extremely challenging because of the heterogeneity of these systems, which is likely to result in a multitude of different active sites.[2] Moreover, the spectroscopic identification of these sites is often challenging because of their very low concentrations, in particular, when similar species are present also as part of the bulk.[3] These problems can be overcome or at least be reduced if the active sites are precisely defined.[4,5] Combining experiments and computations, this is demonstrated in the present work for the oxidation of CO on a single-atom Cu catalyst, supported on a metal–organic framework (MOF) support, which can serve as a model system for a wide range of oxidation reactions.

Recently, we reported on a highly active CO oxidation catalyst comprised of isolated Cu ions supported on a Zr-based MOF, UiO-66,[6] where the individual Cu ions are covalently attached to the vacant terephthalic acid defects in the UiO-66 (Figure 1).[7–10]

[*] Dr. A. M. Abdel-Mageed, Dr. J. Bansmann, Dr. S. Chen, T. Häring, Prof. Dr. R. J. Behm
Inst. of Surface Chemistry and Catalysis, Ulm University
Albert-Einstein-Allee 47, 89081 Ulm (Germany)
E-mail: juergen.behm@uni-ulm.de

Dr. A. M. Abdel-Mageed, Dr. J. Rabeah, Prof. Dr. A. Brückner
Leibniz Institute for Catalysis (LIKAT Rostock)
18059 Rostock (Germany)
E-mail: ali.abdelmageed@catalysis.de

Dr. B. Rungtaweevoranit
Dept. Chemistry and Kavli Energy NanoSciences Institute, University of California
Berkeley, CA 94720 (USA)

Dr. B. Rungtaweevoranit, Dr. S. Impeng, Dr. S. Namuangrak, Dr. K. Faungnawakij
National Nanotechnology Center (NANOTEC), National Science and Technology Development Agency (NSTDA)
Pathum Thani 12120 (Thailand)
E-mail: bunyarat.run@nanotec.or.th
sarawoot.imp@nanotec.or.th

Dr. S. Chen
Inst. Inorganic Chemistry, Kiel University
Max-Eyth-Straße 2, 24118 Kiel (Germany)

Prof. Dr. R. J. Behm
Inst. of Theoretical Chemistry, Ulm University
Oberberghof 7, 89081 Ulm (Germany)

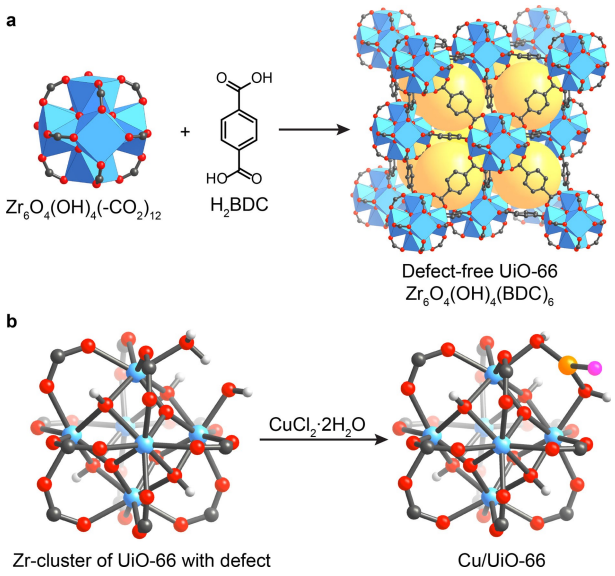

Figure 1. Crystal structure of the UiO-66 support and the Cu/UiO-66 catalyst. a) Defect-free UiO-66, constructed by linking $Zr_6O_4(OH)_4$-$(-CO_2)_{12}$ and H_2BDC (hydrogen atoms are omitted for clarity, and blue polyhedra represent $Zr_6O_4(OH)_4(-CO_2)_{12}$ clusters). b) UiO-66 typically contains missing-linker defects, and these sites are terminated by hydroxyl (and possibly water) groups. These defect sites were used to attach individual Cu atoms by reaction of UiO-66 with $CuCl_2{\cdot}2\,H_2O$. Atom labeling Scheme: C: black; O: red; H: grey; Zr: blue; Cu: orange; Cl: pink.

This system is ideally suited for mechanistic studies since it is structurally well-defined and there are only few types of possible active sites in the open structure of the MOF,[6,11–15] which are also easily accessible to the reactants.[16] This allows for a rigorous correlation of the reactivity with the structural/electronic properties of the catalyst and adsorbed species under working conditions, which in combination with computational modelling leads to detailed insights into the reaction mechanism under these conditions.

To realize this goal, we employed a comprehensive multi-technique approach, combining measurements of the kinetics and of kinetic isotope effects (KIEs) with different operando/in situ spectroscopies, monitoring also the product composition, and with extensive density functional theory (DFT) calculations. While in most studies the DFT calculations concentrate on the determination of the energies of the reaction intermediates and transition states for identifying the most favorable reaction pathway, we here also tested other catalyst properties such as the Cu oxidation and spin state or the vibrational properties of key adsorbates during reaction, as well as the adsorption behavior of the separate reactants, and used the agreement between theory and experiment in these properties as additional guidance in the search for the correct reaction pathway. This comprehensive approach, which distinguishes this work from many other studies, allowed us to map out the complete mechanistic pathway for CO oxidation and identify the different reaction steps and activation barriers. Most important, the reaction involves two dominant activated steps, reactive O_2 dissociation by interaction with co-adsorbed CO, and reaction between a second CO_{ad} and the remaining adsorbed oxygen atom.

Results and Discussion

The Cu/UiO-66 catalyst was synthesized following our previously published protocol.[6] The Cu loading was 2.0 wt %, equivalent to a Cu/Zr_6 node ratio of 0.8, which agrees with the amount of vacant terephthalic acid defect sites. Installation of Cu in UiO-66 does not create additional defects that could potentially act as catalytic sites (see Supporting Information, section 1)

We first explored the dependence of the reaction rate on the reactant concentrations and temperature. Varying the CO partial pressure while keeping the O_2 concentration at 1 % results in an increase in the CO oxidation rate (Figure 2a) (for time-resolved rate measurements see Figure S1, Supporting Information). For different temperatures (250, 180, and 120 °C) we obtained reaction orders with respect to CO (n_{CO}) of 0.8 ± 0.1, 0.9 ± 0.1, and 0.2 ± 0.1, respectively. In a similar set of experiments, changing the O_2 concentration from 1 % to 15 % while keeping the CO concentration at 1 %, we obtained reaction orders with respect to O_2 that are close to zero at 250 °C and 180 °C, and slightly higher (0.2 ± 0.1) at 120 °C (Figure 2b). Under all conditions, the reaction rate is limited by a lack of CO, and almost independent of the O_2 concentration.

Next we determined the apparent activation energy ($E_{a,app}$) of the reaction at $p_{CO}p_{O_2}=1$ in the three different temperature ranges (time-resolved rate measurements see Figure S2, Supporting Information). Overall, we find a curved variation of the logarithmic rate vs. $^1/_T$ (Figure 2c). Such behavior can arise from a number of different reasons, such as a preceding adsorption-desorption equilibrium, a change in rate-determining step with temperature, or also mass transport effects. Considering that we have no indication for mass transport limitations (see Supporting Information section 1, Kinetic measurements, and additional DRIFTS data in Figure S16, Supporting Information) and that a preceding adsorption-desorption equilibrium should result in a decrease of the apparent activation energy with increasing temperature rather than an increase, we favor a change in rate limiting step as most plausible explanation. Evaluating the resulting $E_{a,app}$ values individually, we obtain values of 69.0 ± 3.5, 60.0 ± 3.0, and 28 ± 3.0 kJ mol^{-1} at around 250, 180, and 120 °C, respectively. Based on these results CO adsorption does not result in site blocking for O_2, as often observed for noble metal catalysts such as Pt/Al_2O_3 at lower temperatures,[17] as this would be reflected by a negative reaction order for CO. Furthermore, the reaction of CO_{ad} is likely preceded by reversible adsorption and desorption of at least one of the reactants. Note that as had been demonstrated earlier,[6] the UiO-66 structure is stable under CO oxidation conditions at temperatures up to 350 °C.

KIEs were investigated by comparing the CO oxidation rates in $C^{16}O/^{16}O_2$ and $C^{16}O/^{18}O_2$ under steady-state conditions (reaction rate data in Figure S3, Supporting Informa-

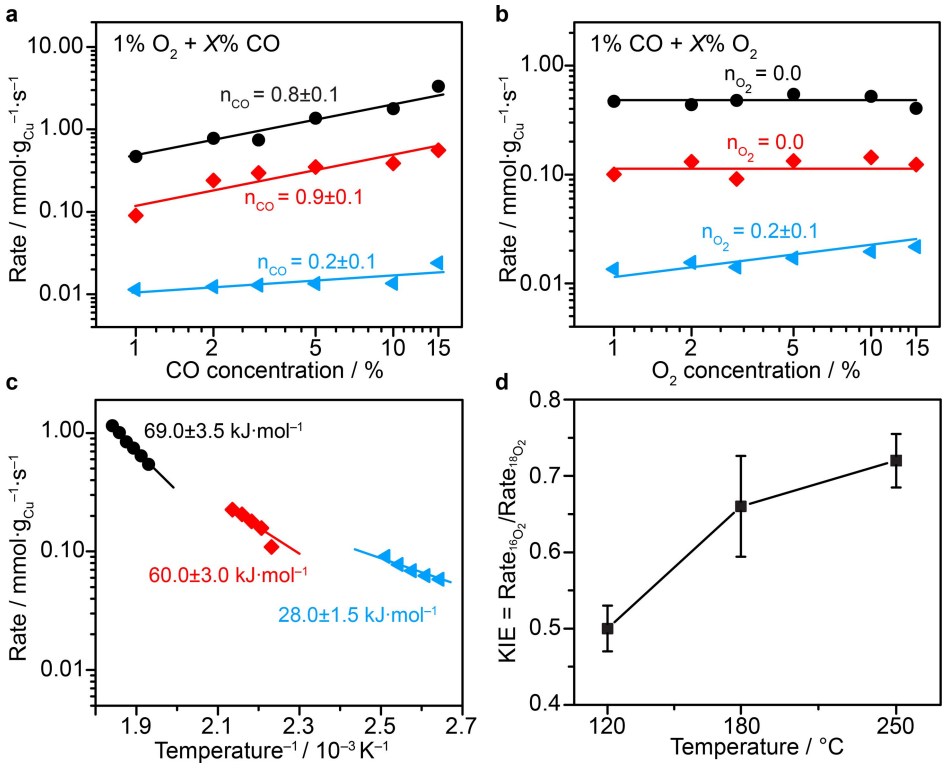

Figure 2. Reaction orders of CO and O_2, apparent activation energies, and kinetic isotope effect (KIE) at different temperatures. a) Cu mass-normalized CO oxidation rates (steady-state conditions) at fixed concentration of O_2 (1%) as a function of the CO concentration (1–15%) at different temperatures (●:250°C; ♦:180°C; ◀:120°C). b) Cu mass-normalized CO oxidation rates (steady-state conditions) at a fixed concentration of CO (1%) as a function of the O_2 concentration (1–15%) at different temperatures (●: 250°C; ■: 180°C; ▲: 120°C). c) Arrhenius plots for determining the apparent activation energies ($E_{a,app}$) in three different temperature ranges (around 250°C, 180°C, and 120°C), measured in a 1:1 ratio of CO:O_2 (1% CO, 1% O_2, balance N_2) after can 1000 min on stream. d) Kinetic isotope effect (KIE), calculated from the ratio of the CO oxidation rates (steady-state conditions) in an about 1:1 gas mixture of CO/$^{16}O_2$ or CO/$^{18}O_2$ (0.95% CO, 0.9% O_2, balance N_2) at a total flow rate of 30 N mL min^{-1}.

tion). To the best of our knowledge, similar measurements have not been reported for CO oxidation before. Changing from $^{12}CO/^{16}O_2$ to $^{12}CO/^{18}O_2$ results in a significant increase of the reaction rate, which corresponds to KIE values of 0.72 ± 0.04, 0.66 ± 0.06, and 0.5 ± 0.03 at 250°C, 180°C, and 120°C, respectively (Figure 2d). Comparable results were obtained also when monitoring the CO_2 formation by IR spectrometry in dynamic, steady-state isotopic transient kinetic analysis (SSITKA) experiments (see Figure S4 and S5, Supporting Information). Given the relatively small difference in the molecular masses, these values are characteristic for a primary inverse KIE,[18,19] indicating that the rate-limiting step involves the breaking/formation of the bond to the respective oxygen atom either in the rate-determining step or in a subsequent slow, product-determining step. Most likely, this refers to the activation of the strong O=O bond (O_2 dissociation), or the removal of an (activated) oxygen species by reaction with CO. Here we would like to note that we assume that all Cu species present are active and do not affect each other, which based on the open structure and the uniform separation between neighboring Cu sites appears reasonable. Even if there were any inert species, this will not affect the mechanistic insights.

To identify the electronic and structural properties of the catalyst during reaction, we first followed the time evolution of the Cu oxidation state of a pre-reduced catalyst in the reaction gas by monitoring changes in the X-ray absorption near-edge spectra (XANES) of the Cu K-edge (spectra see Figure S6a, Supporting Information). Linear combination analysis (LCA) using Cu_2O and CuO as references shows a continuous increase of the Cu^{2+} content during CO oxidation, reaching 90% Cu^{2+} after 400 min on stream (for determination of the 90% Cu^{2+} content see reaction data in Figure S6b and discussion in the Supporting Information). It will be shown later that based on the DFT calculations the Cu charge states are somewhere between Cu^{1+} and Cu^{2+}, depending on the reaction intermediate, and therefore we prefer to use the terms Cu^{1+}-like and Cu^{2+}-like. Also the ratio between Cu^{1+}-like and Cu^{2+}-like species may differ somewhat from that determined for Cu^{1+} and Cu^{2+} species derived by LCA, although the general trends should remain valid. Hence, during reaction the catalyst predominantly consists of Cu^{+2}-like species. This state represents the starting point for subsequent XANES-titration measurements presented below. Similar measurements were performed also at 180°C and 120°C, showing that Cu oxidation during the reaction is increasingly dominant at

these lower temperatures (Figure S7a, Supporting Information).

Analysis of extended X-ray absorption fine structure (EXAFS) spectra recorded together with the XANES spectra at different reaction temperatures (Figure S7b, and details in Figures S8 and S9, Supporting Information) suggests that independent of the temperature the Cu ions bind mainly to O atoms, with a low coordination number of 2.3 ± 0.5 and a mean Cu–O distance of 1.97 ± 0.02 Å, which is significantly longer than the distance in Cu_2O (1.85 Å)[20] and also in the longer range of those in CuO (1.89–2.04 Å).[21] This and the lack of second shell Cu–Cu scattering in the EXAFS data point to the predominant presence of individual Cu ions rather than of oxide particles in the temperature range investigated.[6] Furthermore, the result of a Cu–O coordination of 2.3 ± 0.5, which indicates dominant twofold coordination with some contributions from threefold coordination, fits also nicely with the LCA results and the insights derived from DFT calculations, which will be discussed in more detail later. Considering only the shorter bonds of strongly bound Cu–O and Cu–OH species and not the longer Cu–O_2 bond (see Table S4), several of the intermediates (INT), such as INT I, II and III (see reaction cycle in the DFT calculations part) show such kind of Cu–O coordination. Based on the finding of a dominant Cu^{2+} oxidation state (Figure 3), contributions from the intermediates INT II and INT III, which show charge states of well above 1 (see Table S5 and page S8 for details), must be dominant, while contributions from INT I, which is clearly Cu^{1+}-like, and from the other intermediates with a threefold Cu–O coordination contribute less. As will be discussed later, this fits well also with the DFT results, since one can expect the highest contributions to the spectra from the intermediates preceding the rate-limiting step, which are furthermore commonly considered to be equilibrated.

To further characterize the redox properties of the Cu species we performed titration experiments, recording

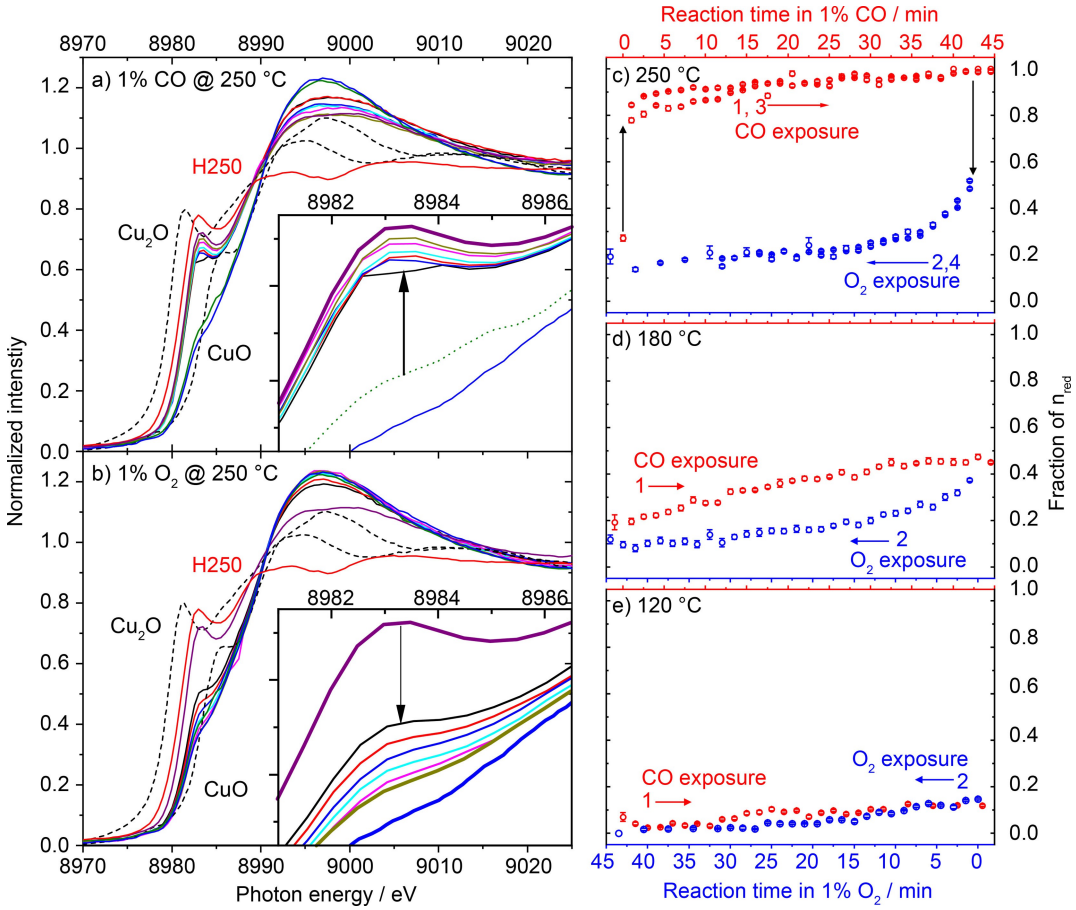

Figure 3. Operando XANES spectra recorded during CO and O_2 titration at different temperatures. a) Sequence of XANES spectra recorded at the Cu K-edge during the titration of the Cu/UiO-66 catalyst in a flow of 1% CO/N_2, following reduction in 10% H_2/N_2 at 250 °C for 1 h (H250), subsequent CO oxidation (1% CO, 1% O_2, N_2 balance) at 250 °C for 900 min and purging in N_2 for 15 min. The initial state of the catalyst for titration at 250 °C, after purging in N_2, is indicated by the first data point in c), before the arrow. b) Subsequent titration of the pre-reduced catalyst using a flow of 1% O_2/N_2. The insets in (a) and (b) show expanded spectra in the range 8981—8986.5 eV, arrows therein indicate the first reduction and oxidation step, respectively. c)–e) Plots of the time-dependence of the LC analysis of the sequence of spectra at 250 °C, 180 °C and 120 °C (see Figure 3a, b and S10, Supporting Information), where the spectra obtained after the first CO reduction at 250 °C and after oxidation at 120 °C were used as references for a "fully reduced" and a "fully oxidized" state.

XANES spectra while sequentially exposing the spent catalyst first to a flow of CO/N_2 and then to O_2/N_2 at 250 °C, after the preceding reaction at 250 °C ($CO:O_2=1:1$) for 900 min. Upon exposure to 1 % CO/N_2, the XANES spectra show a gradual increase of the white line intensity at 8983 eV (Figure 3a, inset), suggesting an initially fast and subsequently slower reduction of the Cu species from Cu^{2+}- to Cu^{1+}-like. But even after 45 min on stream in CO (last spectrum in the sequence), the catalyst is still clearly off from the fully reduced state obtained after H250 treatment, indicating that complete reduction is not possible under these conditions. During subsequent exposure to a flow of 1 % O_2/N_2 (Figure 3b), the Cu species are re-oxidized. In this case, however, Cu oxidation even exceeds the level obtained during CO oxidation, as indicated by the more CuO-like shape of the final spectrum. Repeating this titration cycle results in an essentially identical series of spectra, indicating that reduction and re-oxidation of the catalyst are fully reversible under these conditions. This is illustrated also by LCA fits of the two series, which quantitatively illustrate the temporal progress in Cu^{1+} oxidation and Cu^{2+} reduction (Figure 3c). Repeating the same exposure sequences at lower temperature, at 180 °C, we also observed reversible changes, but with slower and less pronounced oxidation or reduction (Figure 3d, spectra see Figure S10a, b, Supporting Information). At 120 °C, finally, the catalyst essentially remains in the oxidized state obtained at the higher temperatures (Figure 3e, Figure S10c, d, Supporting Information). Note that for 180 °C and 120 °C, titration started after re-oxidation at 250 °C and 180 °C, respectively. These results indicate that with decreasing titration temperature i) the oxidized state reached after O_2 titration is slightly more pronounced and that ii) the reduction of the oxidized state of the catalyst is more hindered.

In total, the XAS data indicate that the mean Cu oxidation state can vary significantly with the reaction temperature, with pronounced changes between oxidized and reduced state at higher temperatures, while at lower reaction temperatures (120 °C) this is not possible, resulting in an increasing tendency for over-oxidation of the catalyst under these conditions.

Operando electron paramagnetic resonance (EPR) measurements were performed to probe changes in the Cu oxidation state, and the formation of EPR-active O-vacancy defects during pretreatment or reaction. After the H_2 pretreatment, the EPR spectrum of the catalyst still exhibits a weak, broad signal of Cu^{2+} ions at $g=2.045$ (Figure 4a, dark blue spectrum), indicating that not all Cu^{2+} ions were reduced to Cu^{1+} upon pretreatment. Additionally, there is a small, but sharp signal at $g=2.005$, which is close to the value often reported for negatively charged O-vacancy defects.[22] Since this peak was also observed for the Cu-free MOF (see Figure S11, Supporting Information), we attribute this to O-vacancy defects in the MOF on sites that are not linked to a Cu ion.

Exposing the catalyst to the CO oxidation gas mixture (1 % CO, 1 % O_2, Ar balance) at 250 °C results in a rapid increase of the axial EPR signals of Cu^{2+} at $g_{||}=2.314$ and

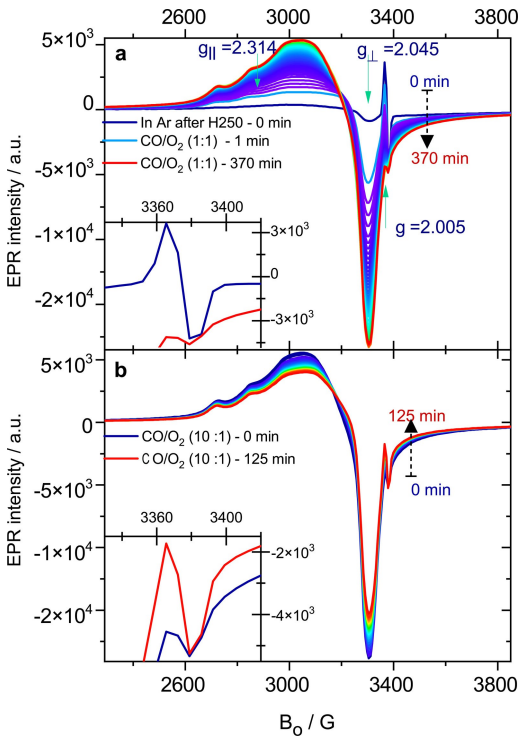

Figure 4. Operando EPR signals recorded during CO oxidation. a) Sequence of time-resolved operando EPR spectra recorded on a pre-reduced (10% H_2/N_2 for 1 h) Cu/UiO-66 catalyst during CO oxidation in a standard reaction mixture (1% CO, 1% O_2, N_2 balance—30 N mL min^{-1}) at 250 °C. b) Sequence of EPR spectra recorded during CO oxidation in a CO-rich gas mixture (10% CO, 1% O_2, N_2 balance—30 N mL min^{-1}) at 250 °C, following the procedure in a). Insets show a magnified detail of the region around 3380 G.

$g\perp=2.045$ (Figure 4a), which are characteristic for Cu^{2+} ions in a tetragonally distorted surrounding ($g_{||}>g\perp>g_e$), where $g_{||}$, $g\perp$ and g_e denote g_z, $g_x=g_y$ and g of the free electron, respectively.[23,24] The clear hyperfine splitting points to structurally well-defined species, which are predominantly formed under reaction conditions. This will be discussed in more detail with the results of the DFT calculations. At the same time, the signal at $g=2.005$ decreased (see inset in Figure 4a). From the growth of the EPR signal of the Cu^{2+} species over more than 350 min on stream (see Figure 4a and S12, Supporting Information) we conclude that the fraction of Cu^{2+} species and thus the mean oxidation state of the Cu ions increased continuously during reaction in a 1:1 gas mixture, leaving the catalyst with a much higher oxidation state than that of the reduced catalyst, well above Cu^{1+}. These findings fit very well with our XANES results, showing the slow oxidation of Cu^{1+}- to Cu^{2+}-like sites for over 350 min. This also provides a simple explanation for the initial activation phase of Cu/UiO-66 during the reaction. Consistent with these findings, we also observed that changing to reaction atmospheres with higher CO- (see Figure 4b and inset therein) or O_2-contents (see Figure S13, Supporting Information) during reaction at 250 °C or to a pure CO/Ar atmosphere after the CO oxidation at 250 °C in a 1:1 reaction mixture (see Figure S14,

Supporting Information) leads to a similar increase/decrease of the Cu^{2+}-like signal and of the signal at g = 2.005. Finally, further titration experiments performed at 120 °C also confirm that reduction of the catalyst, after reaction at 250 °C, is not possible at 120 °C (Figure S15, Supporting Information).

Overall, the EPR findings confirm our XANES-based conclusion that the mean Cu oxidation state can vary significantly with the $CO:O_2$ ratio and also depending on the temperature and that at lower temperatures (120 °C) reduction of the spent catalyst is not possible.

To support our above conclusions, we performed in situ infrared spectroscopy (diffuse reflectance Fourier transform IR spectroscopy, DRIFTS) measurements of the CO adsorption characteristics under different reaction conditions (Figure 5a–c). Here it is important to note that the CO-FTIR signal is considered to be only sensitive for adsorption on Cu^{1+}-like species under these conditions,[25] which according to the XANES-LCA represent a minority of the Cu sites, while EPR is only sensitive to Cu^{2+} species. Summarizing the main trends obtained for reaction at 250 °C we find i) a general decay of the CO_{ad} related bands with increasing O_2 concentration at constant CO concentration, and ii) an increase in the CO_{ad} related intensity with increasing CO concentration, when the O_2 concentration was kept at 1 %. Furthermore, we could iii) identify a number of different CO_{ad} related bands at around 2122, 2133 and 2138 cm^{-1}, whose intensity responds in different ways to changes in the reaction conditions. These bands closely resemble our previous findings for reaction in a 1:1 mixture at 250 °C,[6] where a peak at 2113 cm^{-1} was attributed to CO adsorption on Cu^{+1} ions in a freshly reduced catalyst, while peaks at about 2118 and 2132/2138 cm^{-1} were associated with CO adsorption on Cu^{1+} species in the presence and absence of coadsorbed oxygen during later stages of the reaction.

Redoing this experiment at 180 °C, the general trends are similar, with differences in details, in particular with higher intensities in the CO_{ad} related bands (see Figure 5d–f). For reaction at 120 °C (Figure 5g–i), the CO_{ad} band intensities are again much higher than at the higher temperatures, although based on the XANES data the concentration of Cu^{1+}-like species is lower under these conditions than during reaction at 250 °C (Figure 3). Apparently, this loss is overcompensated by a much higher relative population of Cu^{1+}-like sites by CO_{ad} species. Also in this case, the

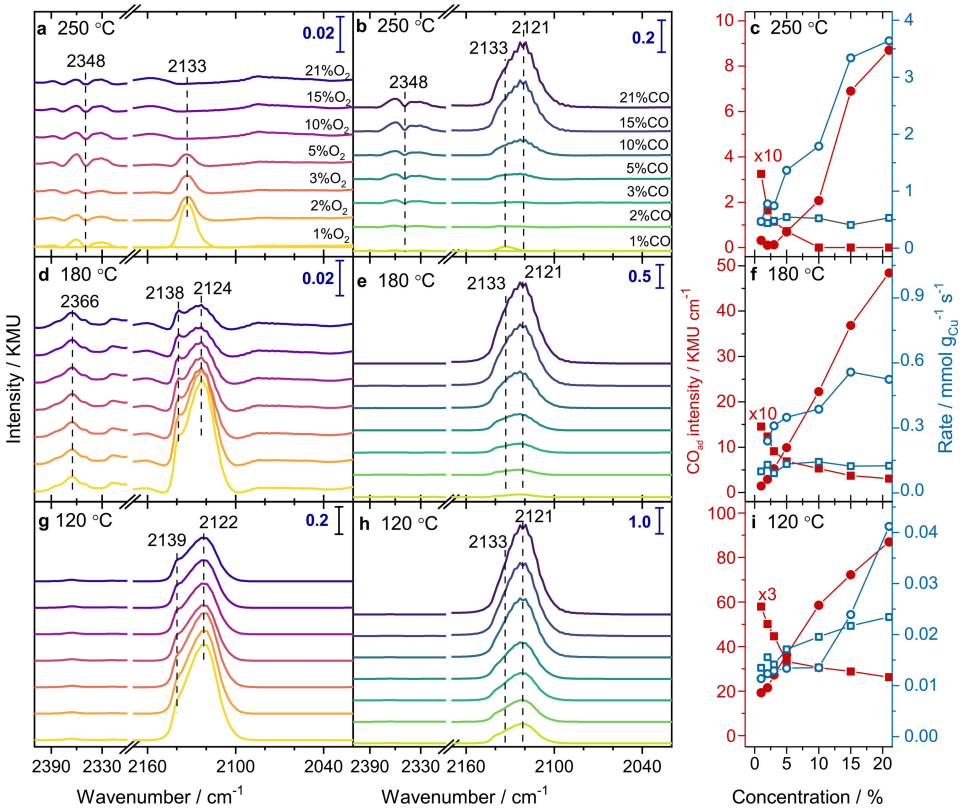

Figure 5. In situ DRIFTS measurements on the Cu/UiO-66 catalyst during exposure to the reaction gas mixture at different temperatures. a), d), g) In situ DRIFT spectra collected at fixed CO concentration (1 %) while varying the O_2 content (1–21 %) at different temperatures (a): 250 °C, d): 180 °C, g): 120 °C). b), e), h) In situ DRIFT spectra collected during CO oxidation at a fixed concentration of O_2 (1 %) as a function of the CO concentration (1–21 %) at different temperatures (b): 250 °C, e): 180 °C, h): 120 °C). c), f), i) Integrated intensities of the CO_{ad} related absorption band (2170–2080 cm^{-1}) (left axis) and reaction rates (right axis), which were determined separately in kinetic measurements under identical conditions, as a function of CO and O_2 concentration at different temperatures (c): 250 °C, f): 180 °C, i): 120 °C). Filled red symbols (●,■) represent CO_{ad} intensities, while empty blue symbols (□,○) represent rates; squares refer to fixed CO and varying O_2 concentrations; circles represent fixed O_2 and varying CO concentrations.

peaks represent two contributions. Both upon varying the O_2 concentration or varying the CO concentration, the relative contribution of the high-frequency band,is lower than at 180 °C in the same gas mixtures (Figure 5g–i), independent of the reaction atmosphere. The lower intensity of the high-frequency band can be explained if the formation of the related species requires an activated step, in agreement with conclusions from the activation energy results. The close correlation between CO absorption intensity and thus CO_{ad} coverage on the one hand and reaction rates on the other hand under different conditions is displayed quantitatively in the right panels of Figure 5

In combination with the XAS and EPR data, the DRIFTS results lead to a much more detailed mechanistic picture. Under most reaction conditions we find contributions from two states, one with a maximum at 2122 cm^{-1} and one with a maximum at 2138 cm^{-1}, indicating that both states are populated under these reaction conditions. The previous assignment of the higher frequency shoulder with a maximum at 2138 cm^{-1} to CO coadsorbed with oxygen fits well to the trend observed in the present data, where the relative contribution of this state increases with increasing relative O_2 concentration. On the other hand, the observation of a decreasing total CO_{ad} intensity with increasing O_2 content, while the CO_2 formation rate remains constant (no enhanced reactive removal of CO_{ad}), indicates that under these conditions an increasing fraction of the Cu sites is not accessible to CO adsorption anymore. This may point to an increasing fraction of weakly binding, possibly more Cu^{2+}-like sites.

Considering that measurable CO adsorption on Cu^{2+} sites is only possible at temperatures below 100 K,[25] we infer that throughout the reaction cycle there are considerable amounts of more Cu^{1+}-like species available for CO adsorption, independent of the reaction temperature. Based on the DRIFTS data, the variations in the nature of the Cu sites do not only correspond to changes between Cu^{2+}- and Cu^{1+}-like species, but involve (also) variations between different Cu^{1+}-like sites. In CO-rich atmosphere, contributions from a more reduced Cu^{1+}-like state were considerably higher. Similar discrepancies are obtained for reaction at 120 °C, where XANES and EPR data indicated a largely oxidized Cu^{2+}-like state, rather similar to that in CuO, while the DRIFTS spectra indicate that also under these reaction conditions CO adsorption is still possible, actually with a rather high coverage (see Figure 5g, h). The high CO_{ad} coverage can be explained by the much lower desorption rate under these conditions, together with a very low rate for reactive removal of CO_{ad}. The fact that the different band positions hardly change with increasing O_2 concentration indicates that the nature of the Cu species carrying an adsorbed CO is not affected much by the excess O_2 in the gas phase, only their relative contributions. For a more quantitative interpretation, we fitted the FTIR peak by two different components, one at lower wavenumber (LW, 2121–2124 cm^{-1}) and one at higher wavenumber (HW, 2133–2138 cm^{-1}) (see Figure S17), which as discussed before can be attributed to CO_{ad} on Cu^{1+} sites co-adsorbed with oxygen (HW-band) and without co-adsorbed oxygen (LW-band) (see ref. [25] and calculated frequencies in Figure 6). This fully confirms our previous conclusion that the FTIR spectra can be explained by contributions from two states which are electronically different, most likely from the INT II and INT III intermediates. Focusing on the width of these bands, we obtained values of about 19 ± 1 cm^{-1} (LW) and of 11 ± 2.5 cm^{-1} (HW) for the FWHM of the respective components at different temperatures, except for the $CO:O_2 = 1:1$ gas mixture at 250 °C, while the relative intensities depended on the reaction conditions. FWHM values of 10–14 cm^{-1} are typical for CO_{ad} on highly homogeneous surfaces, while the larger value of the LW component may point to slight differences between CO_{ad} species in that component, e.g., due to contributions from different intermediate states (see more details in Table S3, Supporting Information).

Finally, we performed DFT calculations of the reaction using a cluster model of the catalyst. Different from two recent studies on CO oxidation on MOF-based catalysts,[26,27] we calculated not only energy levels of possible reaction intermediates and transition states, but evaluated also other catalyst/reactant properties at the individual reaction stages such as oxidation/spin states or vibrational properties for mapping out the reaction pathway. The cluster model is based on the single crystal structure of UiO-66, where the BDC linkers are replaced by acetate groups to reduce the computational time, and corroborated by elaborate characterization. Based on the experimental data reported in our previous study,[6] the as-synthesized Cu/UiO-66 catalyst contains Cu^{1+} ions bound to the –OH (and possibly-OH_2) ligands capping the defect sites of the Zr-node of UiO-66, and a Cl^- ligand. This results in a model system of the composition $Zr_6O_4(OH)_4(acetate)_{11}(OH)_2CuCl$, Cu/UiO-66 (see Figure 1), which after the H_2 pretreatment loses its Cl^- ligand. This leads to two-fold coordinated Cu, bound to the oxygen atom of an OH ligand of the neighboring Zr^{4+} ion and to the threefold coordinated μ_3-O atom capping the Zr-node. Accordingly, an O-vacancy on a coordinatively unsaturated Zr ion (Zr_{cus}) is formed. Part of this cluster, which will also serve as energy reference, is displayed as intermediate INT I in Figure 6. Based on a detailed analysis of a large number of possible reaction steps we arrived at a reaction cycle (Figure 6), whose main steps will be summarized in the following:

Exposing the catalyst to the reaction mixture can result in either adsorption of CO or O_2. Starting with CO adsorption, the calculated adsorption energy on the Cu site is -209 kJ mol^{-1}, while CO adsorption on the Zr_{cus} site was found to be unstable, relaxing spontaneously by moving to the Cu site. This may be followed by adsorption of an O_2 molecule, which preferably also binds to the Cu site, resulting in intermediate III with a relative energy of -244 kJ mol^{-1}. The same intermediate can be reached also by first O_2 adsorption, followed by CO adsorption. Subsequently, the adsorbed CO molecule can react with the co-adsorbed O_2 via a transition state (TS I) with an activation barrier of 141 kJ mol^{-1} (INT III→TS I→ INT IV), resulting in the intermediate IV with a weakly adsorbed CO_2 and the remaining O atom. The latter O atom is located between

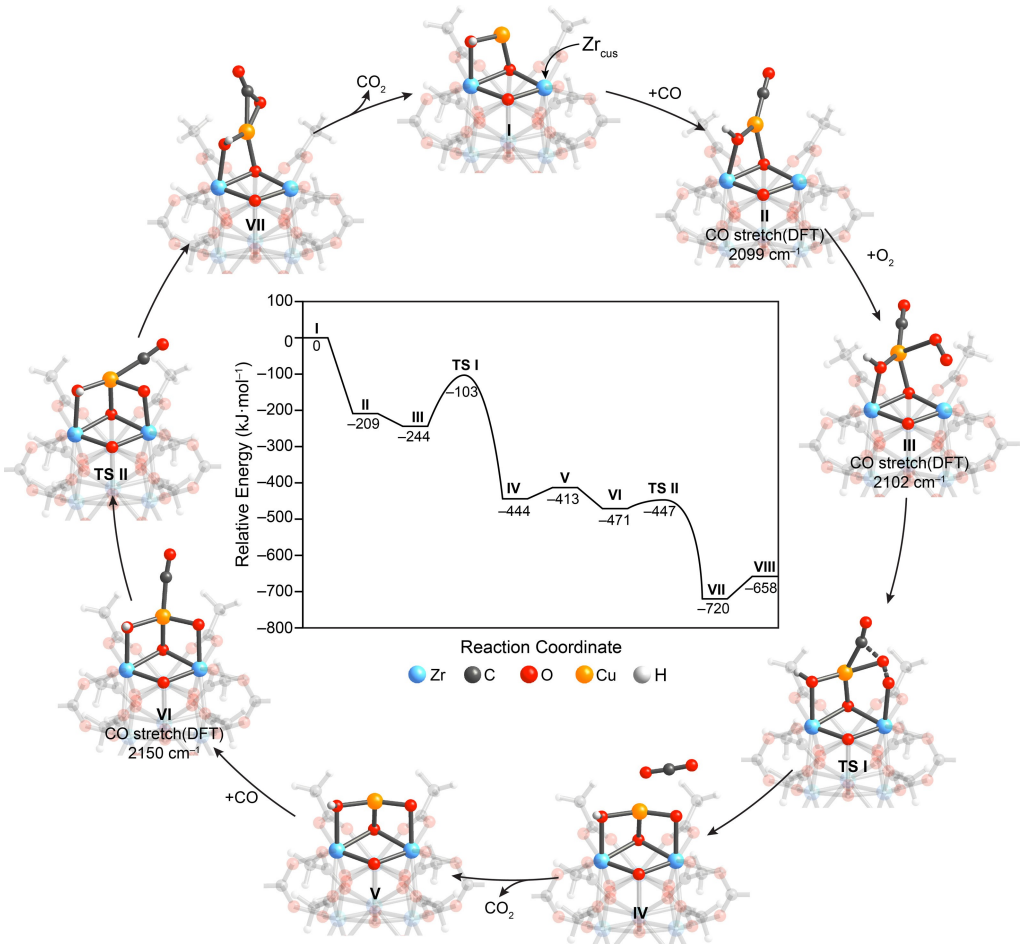

Figure 6. Reaction cycle with optimized structures for intermediates (I–VII) and transition states (TS I, II) for CO oxidation by O_2 on the Cu/UiO-66 catalyst (see also a tested, but improbable cycle in Figure S18), and the energy pathway for this reaction pathway.

Zr_{cus} and Cu ion, binding to these two atoms. The Cu–O distances obtained from the DFT calculations for this intermediate, 1.91 Å (Cu–O in OH) and 1.89 Å (Cu–O for μ_3-O), agree very well with the results from the EXAFS evaluation (1.97 ± 0.02 Å). Rather similar bond lengths are obtained also for INT I and INT II (see Table S4, Supporting Information), while the Cu–O distance to the adsorbed O_2 is much larger (2.3 Å). Next, the adsorbed CO_2 molecule desorbs (energy increase 31 kJ mol^{-1}), reflecting the weak bonding of CO_2 to the active Cu site (Cu···CO_2 distance 2.41 Å). Note that the resulting intermediate V is not identical to the initial cluster INT I, due to the remaining O atom. Thus, the resulting energy decay of 413 kJ mol^{-1} describes the energy gain for the oxidation of one CO molecule plus filling the O-vacancy ($\square_{O\text{-}vac}$) between the Cu site and the neighboring Zr ion with a bridging O atom (O_{br}): $CO + O_2 + \square_{O\text{-}vac} \rightarrow CO_2 + O_{br}$. This results in a Cu ion with an electron configuration $Cu = 4\,s^{0.32}3d^{9.45}4p^{0.03}$ (triplet spin state, see section S7.4 in the Supporting Information), i.e., with a charge state that is higher than that of the bare cluster, thereby assigned as a Cu^{2+}-like ion. Note that the charge states of these Cu ions do not correspond to pure Cu^{1+} or Cu^{2+} states, but rather show fractional charges that that as mentioned before are best described as Cu^{1+}-like and Cu^{2+}-like. Checks of the reliability of these calculated charge states using a 1,4-benzenedicarboxylate (BDC) cluster as Zr-node and a quantum chemistry software (ORCA) confirmed these trends (see section S7.3 and Table S5, Supporting Information).

The second CO oxidation reaction begins with the adsorption of a second CO molecule on the Cu^{2+}-like ion, leading to the intermediate VI (adsorption energy 58 kJ mol^{-1}). The adsorbed CO molecule then reacts with the remaining O_{br} atom via the transition state TS II with an activation energy of 24 kJ mol^{-1} to form the second CO_2 product (intermediate VII). Hence, this barrier is considerably smaller than that in the first oxidation step. Finally, this CO_2 species desorbs with an activation energy of 62 kJ mol^{-1} (VII→I), which finishes the second CO oxidation step and frees the Cu single-atom active center for the next reaction cycle. Overall, the CO oxidation cycle is exothermic by 658 kJ mol^{-1}, which is reasonably close to the well-known thermodynamic reaction enthalpy of −565 kJ mol^{-1}.

Based on the size of the activation energy, the reactive dissociation of O_2, upon reaction with coadsorbed CO, can

be considered as the rate-determining step. This fully agrees with our observation of a sizeable ^{18}O-KIE, since O–O–bond breaking is involved in that reaction step (from INT III via TS I to INT IV). Here it is important to realize that this barrier height cannot be directly compared with the experimentally determined apparent activation barrier, as the latter involves also contributions from reactant adsorption/desorption. The discrepancy between the calculated barrier heights (about 141 kJ mol^{-1}) and the experimentally determined apparent activation energies (28–69 kJ mol^{-1}) and also the temperature dependence of the latter values (Figure 2c) are not unexpected for a multi-step process. Furthermore, considering the rather low adsorption energy of CO in intermediate VI, it is not surprising that the reaction is mainly limited by a lack of CO_{ad}, at least at the higher temperatures, which is reflected by the reaction order for CO of close to 1, while that for O_2 is almost zero. The reaction cycle derived here is also supported by the close agreement between the trends of the calculated C–O frequencies (see Figure 6) and those observed experimentally.

Finally, we addressed the question whether we can also explain the reversible oxidation and reduction of the catalyst when exposing it to solely O_2 or CO containing gas mixtures (see Figures 3 and S10, Supporting Information), and the change in oxidation state and spin state observed experimentally. Main results of these calculations were that i) the catalyst can indeed be oxidized by dissociative adsorption of O_2 on the Cu site, resulting in metastable structures with 2 adsorbed O_{ad} per Cu atom (activation barrier 175 kJ mol^{-1}, see Figure S19, Supporting Information), and that ii) upon exposure of these structures to CO they can be reduced again, where the reduction process is slower than oxidation. iii) Evaluation of the spin densities in the different intermediates (details see section S7.4, Supporting Information) finally revealed that there is no spin density on the Cu atoms in the intermediates INT I (bare cluster) and INT II (after CO adsorption on the Cu site), while there is spin density on these atoms after O_2 co-adsorption on the Cu site (intermediate III) and finally also for the intermediate V, which is reached after reactive removal of the first oxygen atom (see Figure S20, Supporting Information). This means that while we would not expect an EPR signal of Cu for the reduced catalyst or after CO adsorption, this should appear during reaction, as a result of the population of the different intermediates, and also for the oxidized states INT A2 and INT B2 (see Figure S19, Supporting Information), in good agreement with the trends observed experimentally.

Furthermore, we expect that this oxidized Cu state can also be reached during reaction in a 1:1 CO/O_2 gas mixture, due to spontaneous dissociation of the adsorbed $O_{2,ad}$ species instead of reaction of $O_{2,ad}$ with CO_{ad}. Together with the reaction intermediate INT III, the resulting, structurally well-defined species INT A2 or INT B2 are mainly held responsible for the Cu signal in the EPR spectra and its pronounced hyperfine splitting, and also for the Cu^{2+}-like signature observed in XANES. These latter species, which are not part of the main reaction cycle in Figure 6, represent reaction intermediates in a minority pathway which based on the high barrier (Figure S19c, Supporting Information) contributes only little to the reaction. Nevertheless, they essentially dominate the Cu^{2+} EPR spectra and also the XAS spectra under present reaction conditions.

Finally, comparing with traditional reaction pathways, the reaction mechanism derived here for CO oxidation is most closely related to a Mars-van Krevelen mechanism, involving the reversible removal and replenishment of bridging oxygen species.

Conclusion

With the aid of detailed experimental and theoretical evaluation of numerous features during reaction, such as Cu oxidation and spin states, CO_{ad} vibrational characteristics and kinetic isotope effects, we could show that CO oxidation on the molecularly well-defined Cu/UiO-66 MOF with isolated, individual Cu^{1+}-like single-atom sites proceeds via an activated reaction between CO_{ad} and $O_{2,ad}$ species. This is also the most highly activated and thus rate-determining reaction step in the dominant reaction pathway. The adsorbed reactants are both coordinated to the Cu ion. This reaction step leaves a bridged oxygen species on the catalyst, connecting Zr^{4+} and Cu ions, which in a second activated reaction step is removed as well, by adsorption of another CO on the Cu ion and subsequent reaction. For each reaction cycle, reactant adsorption, reactive O_2 dissociation and reaction with CO occur at the same active Cu site, which is distinctly different from traditional bimolecular reaction mechanisms on catalyst surfaces, where these steps mostly occur at different sites, followed by surface diffusion and surface reaction. Spontaneous dissociation of $O_{2,ad}$ and subsequent reaction of CO_{ad} with the resulting atomic oxygen species are also possible, but strongly hindered and do not contribute significantly to the reaction rate. They dominate, however, the EPR spectra, and contribute significantly to the XAS spectra. In contrast, the FTIR spectra are dominated by the states INT II and INT III. The detailed agreement between theory and experiment, including not only calculated energies of reaction intermediates and transition states, but a number of different properties, has led to a detailed understanding of the reaction mechanism under present reaction conditions, which because of the highly identical reaction sites is expected to be valid also for realistic catalyst material and reaction conditions. The comprehensive character of this study can serve as a model for a wide range of catalytic oxidation reactions under relevant reaction conditions.

Acknowledgements

B.R., S.I., S.N. and K.F. acknowledge financial support from the National Nanotechnology Center (NANOTEC), National Science and Technology Development Agency (NSTDA), Thailand (grant number P1851755). We also thank Nanoscale Simulation Laboratory at National Nanotechnology Center (NANOTEC) and NSTDA Supercom-

puter center (ThaiSC) for providing computational resources, as well as the Deutsche Elektronen-Synchroton (DESY, Hamburg, Germany) and Elettra Sincrotrone (Trieste, Italy), who both provided beam time and financial support (project CALIPSOplus under Grant Agreement 730872 from the EU Framework Programme for Research and Innovation HORIZON 2020). Finally, we would like to thank the beamline staff for their help in the XAS measurements and Prof. O. Yaghi (UC Berkeley) for his valuable comments. Open Access funding enabled and organized by Projekt DEAL.

Conflict of Interest

The authors declare no conflict of interest.

Data Availability Statement

The data that support the findings of this study are available from the corresponding author upon reasonable request.

Keywords: Density Functional Theory · Metal–Organic Frameworks · In Situ/Operando Spectroscopies · Reaction Mechanisms · Single-Atom Catalysts

[1] J. K. Nørskov, T. Bligaard, B. Hvolbaek, F. Abild-Pedersen, I. Chorkendorff, C. H. Christensen, *Chem. Soc. Rev.* **2008**, *37*, 2163.
[2] M. Boudart, *J. Am. Chem. Soc.* **1952**, *74*, 3556.
[3] G. Ertl, *Angew. Chem.* **1990**, *102*, 1258.
[4] H. Furukawa, K. E. Cordova, M. O'Keeffe, O. M. Yaghi, *Science* **2013**, *341*, 1230444.
[5] O. M. Yaghi, M. J. Kalmutzki, C. S. Diercks, *Introduction to Reticular Chemistry: Metal-Organic Frameworks and Covalent Organic Frameworks - Front Matter*, Wiley-VCH, Weinheim **2019**, pp. i–xxxix.
[6] A. M. Abdel-Mageed, B. Rungtaweevoranit, M. Parlinska-Wojtan, X. Pei, O. M. Yaghi, R. J. Behm, *J. Am. Chem. Soc.* **2019**, *141*, 5201.
[7] J. H. Cavka, S. Jakobsen, U. Olsbye, N. Guillou, C. Lamberti, S. Bordiga, K. P. Lillerud, *J. Am. Chem. Soc.* **2008**, *130*, 13850.
[8] L. Valenzano, B. Civalleri, S. Chavan, S. Bordiga, M. H. Nilsen, S. Jakobsen, K. P. Lillerud, C. Lamberti, *Chem. Mater.* **2011**, *23*, 1700.
[9] C. A. Trickett, K. J. Gagnon, S. Lee, F. Gandara, H. B. Bürgi, O. M. Yaghi, *Angew. Chem. Int. Ed.* **2015**, *54*, 11162.
[10] S. Ling, B. Slater, *Chem. Sci.* **2016**, *7*, 4706.
[11] S. Yuan, Y.-P. Chen, J. Qin, W. Lu, X. Wang, Q. Zhang, M. Bosch, T.-F. Liu, X. Lian, H. C. Zhou, *Angew. Chem. Int. Ed.* **2015**, *54*, 14696.
[12] Z. Li, A. W. Peters, V. Bernales, M. A. Ortuño, N. M. Schweitzer, M. R. DeStefano, L. C. Gallington, A. E. Platero-Prats, K. W. Chapman, C. J. Cramer, L. Gagliardi, J. T. Hupp, O. K. Farha, *ACS Cent. Sci.* **2017**, *3*, 31.
[13] I. S. Kim, Z. Li, J. Zheng, A. E. Platero-Prats, A. Mavrandonakis, S. Pellizzeri, M. Ferrandon, A. Vjunov, L. C. Gallington, T. E. Webber, *Angew. Chem. Int. Ed.* **2018**, *57*, 909.
[14] K. Otake, Y. Cui, C. T. Buru, Z. Li, J. T. Hupp, O. K. Farha, *J. Am. Chem. Soc.* **2018**, *140*, 8652.
[15] C. Xu, Y. Pan, G. Wan, H. Liu, L. Wang, H. Zhou, S. H. Yu, H. L. Jiang, *J. Am. Chem. Soc.* **2019**, *141*, 19110.
[16] J. Y. Lee, O. K. Farha, J. Roberts, K. A. Scheidt, S. B. T. Nguyen, J. T. Hupp, *Chem. Soc. Rev.* **2009**, *38*, 1450.
[17] M. J. Kahlich, H. A. Gasteiger, R. J. Behm, *J. Catal.* **1997**, *171*, 93.
[18] C. E. H. Bawn, G. Ogden, *Trans. Faraday Soc.* **1934**, *30*, 432.
[19] X. Gao, X. Y. Yu, C. R. Chang, *Phys. Chem. Chem. Phys.* **2022**, *24*, 15182.
[20] E. Ruiz, S. Alvarez, P. Alemany, R. A. Evarestov, *Phys. Rev. B* **1997**, *56*, 7189.
[21] S. Asbrink, A. Waskowska, *J. Phys. Condens. Matter* **1991**, *3*, 8173.
[22] H. Liu, L. Feng, X. Zhang, Q. Xue, *J. Phys. Chem.* **1995**, *99*, 332.
[23] B. J. Hathaway, D. E. Billing, *Coord. Chem. Rev.* **1970**, *5*, 143.
[24] G. A. van Albada, W. J. J. Smeets, N. Veldman, A. L. Spek, J. Reedijk, *Inorg. Chim. Acta* **1999**, *290*, 105.
[25] K. Hadjiivanov, H. Knözinger, *J. Catal.* **2000**, *191*, 480.
[26] S. Guo, Y. Zhao, C. Wang, H. Jiang, G. J. Cheng, *ACS Appl. Mater. Interfaces* **2020**, *12*, 26068.
[27] W. Xue, X. Song, D. Mei, *J. Phys. Chem. C* **2021**, *125*, 17097.

Manuscript received: February 8, 2023
Accepted manuscript online: April 19, 2023
Version of record online: June 14, 2023